SCIENTIFIC Publishing Limited

Electrical Engineering and Technology
http://ojs.ukscip.com/index.php/eet

Article

Graphene Nanoribbon-FET for Higher Drive Current Using Machine Learning-Enhanced First Principles Analysis

Abhay Pratap Singh [1], **Sai Shirov Katta** [2], **R. K. Baghel** [1] and **Shailendra Yadav** [3,*]

[1] Department of Electronics and Communication Engineering, Maulana Azad National Institute of Technology, Bhopal 462003, India

[2] Department of Electrical Engineering, Indian Institute of Technology, Patna 801106, India

[3] Department of Electronics and Communication Engineering, Indian Institute of Technology, Roorkee 247667, India

[*] Correspondence: shailendra_y@ece.iitr.ac.in or abhaysolanki3@gmail.com

Received: 1 April 2025; **Revised:** 11 May 2025; **Accepted:** 25 May 2025; **Published:** 2 June 2025

Abstract: This work presents a novel and innovative design approach for Graphene Nano-Ribbon Field Effect Transistors (GNR FETs), uniquely employing Zigzag Graphene Nano-Ribbons (ZGNRs) as electrodes and Armchair Graphene Nano-Ribbons (AGNRs) as the channel region. To deeply understand device performance, rigorous first-principles modeling was conducted, leveraging Extended-Hückel formalism alongside Landauer-Buttiker transport theory. Extensive Technology Computer-Aided Design (TCAD) simulations systematically explored the impact of critical parameters such as doping concentration (N_D), gate voltage (V_g), and drain voltage (V_d) on transistor behavior. However, the computational intensity associated with such comprehensive analyses necessitated the introduction of an advanced Machine Learning (ML)-assisted methodology, specifically employing a Conventional Artificial Neural Network (C-ANN). Remarkably, this ML-driven strategy achieved highly accurate results within significantly reduced computational times of just 80–90 seconds, underscoring its practicality and efficiency. Furthermore, the intrinsic 2.71 eV band gap of the pristine AGNR channel was effectively modulated in a broad range (0.013–1.6 eV) through controlled doping and engineered defects. An N-passivated AGNR FET demonstrated an extraordinary 157 times enhancement in drive current, although its negligible band gap raised concerns regarding leakage currents. Alternatively, the N-doped Stone-Wales AGNR FET provided a well-balanced performance with a 33.21 nA drive current and a suitable 0.58 eV band gap, substantially reducing leakage risks, enhancing thermal stability, and improving peak inverse voltage robustness. This pioneering ML-assisted C-ANN approach highlights significant potential for accelerating accurate and reliable nano-transistor analyses.

Keywords: Graphene Nanoribbons (GNR); Stone-Wales (SW) Defect; Non-Equilibrium Green's Function (NEFG); First Principle Modeling; Machine Learning (ML)

1. Introduction

Scaling of the transistors to attain switching devices with low power consumption, compact size, and high-performance is indeed the primary goal of VLSI industry. The continuous miniaturization of silicon Metal-Oxide-Semiconductor (MOS) transistors to achieve this goal has already resulted in sub-10 nm silicon technologies where the scale down of silicon below 5 nm is extremely difficult owing to the quantum confinement and dominant short

https://doi.org/10.54963/eet.v1i1.1283

channel effects such as drain-induced barrier lowering (DIBL), hot electron effect, subthreshold leakage, etc. [1]. To enable the further progress of VLSI industry, several alternate materials are being analyzed by the researchers around the globe to replace silicon, such as carbon nanotubes, graphene nanoribbons (GNRs), nanowires, etc. Among these, GNRs which are the 1-dimensional (1-D) derivatives of the graphene stand as promising candidate for the design of next generation nano-devices owing to their remarkable electronic properties and reduced short channel effects [2–6]. Doping is widely explored by the researchers to alter the properties of GNRs for various applications. To discuss a few, Ren et al. [7] reported that the N-passivation of Armchair GNR (AGNR) (N = 18) results in semi-conducting to metallic transition, which can be attributed to several factors. As per their report, the band above the Fermi level is filled by the nitrogen's $2p_z$ electrons, raising the Fermi level. Nguyen et al. [8] synthesized the S-passivated AGNR with N = 13 on Au (111) surface, and observed significant variations in the electronic properties. Likewise, the boron doped AGNRs are synthesized on the Au (111) surface elsewhere [9]. Though, there are several reports on the precise synthesis and characterization of AGNRs, a very few reports are available on the Zigzag GNRs (ZGNR) due to its challenging experimental realization as the Ullmann-type coupling usually takes place in the armchair direction of graphene [10]. Ruffieux et al. [11] synthesized ZGNRs via the bottom-up synthesis approach enabled by the surface-assisted polymerization and cyclodehydrogenation, and observed the edge-localized states via scanning tunnelling spectroscopy. These AGNRs and ZGNRs are widely explored for the design of nanoscale transistors. Rui et al. [12] reported the first principles-based modelling of nanoscale field effect transistor (FET) using boron and phosphorous co-doped AGNR. Lin et al. [13] fabricated a few layer GNR FET by unzipping the carbon nanotubes, and reported high ON/OFF current and mechanical stability at room temperature. Hur et al. [14] reported the theoretical investigations into AGNR FET by formulating a self-consistent Non-Equilibrium Green's Function (NEGF) and reported its suitability for switching applications. Though, several such reports are available, they are mostly made up of AGNRs entirely. However, in this work, we report FETs with AGNR (W = 4) as channel and ZGNR (W = 5) as source/drain electrodes. The choice of AGNRs for the channel and ZGNRs for the electrodes is made based on the fact that former is mostly semiconducting and the latter are mostly metallic. Furthermore, defects and near valence dopants at various sites (N-doping, BN co-doping, N-passivation, Stone-Wales (SW) defect, and N doping at SW defect) are considered in the AGNR channel to tune the electronic properties and enhance the device performance. **Figure 1** illustrates a Graphene Nanoribbon Field-Effect Transistor (GNR-FET) and its electronic behaviour under bias. Subfigure (a) shows the physical structure, while subfigure (b) provides insight into the electronic energy band diagram governing charge transport.

Neural networks offer a valuable tool for modelling the behaviour and characteristics of MOSFETs using experimental data. By training a neural network with a substantial dataset of measured electrical responses such as I_d-V_g curves, the network can learn to approximate the intricate relationship between input parameters (e.g., V_{gs}, V_{ds}) and the corresponding device behaviour. This approach proves advantageous in parameter extraction and modelling, as it enables accurate predictions based on experimental observations, leading to more efficient and effective device characterization and analysis [15,16].

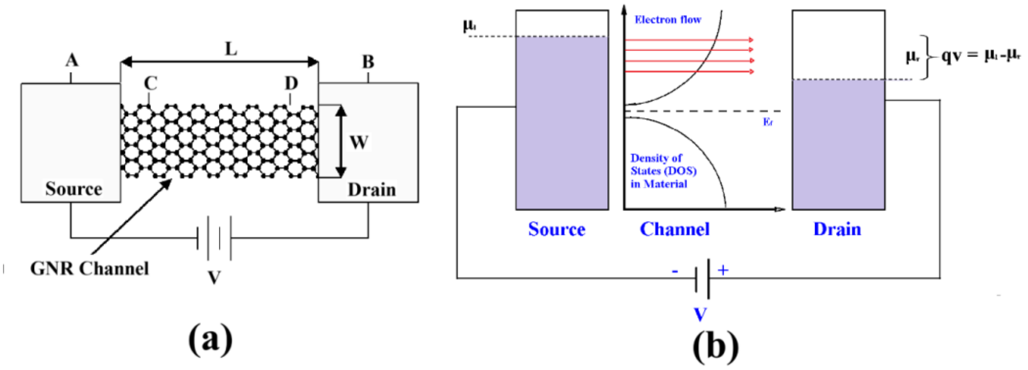

Figure 1. (**a**) Schematic and Equivalent circuit of GNR-FETs device (**b**) Charge flow in GNR-FETs device.

2. Computational Details

The computations are performed using the semi-empirical Extended Huckel formalism and Non-Equilibrium Green's Function (NEGF) formalism as implemented in the Synopsys-Quantum ATK code. The generalized gradient approximation (GGA) exchange correlation functional and k-point sampling of 1 × 1 × 100 have been employed. The structural relaxations are performed using the limited memory Broyden–Fletcher–Goldfarb–Shanno (L-BFGS) algorithm [17] so as to achieve the force and stress tolerance of 0.05 eV/Å and 0.05 eV/Å^3, respectively. The FET construction is made utilizing the silicon dioxide (SiO_2) gate dielectric ($\mathcal{E}_r$ = 3.9). The various properties of the nanoribbons such as electronic band structure, density of states (DOS), and charge transfer are studied before proceeding to the extraction of current-voltage (I–V) characteristics using the Landauer-Buttiker formula [18] given below.

$$I = \frac{2q}{h}\int_{\mu_L}^{\mu_R} [f(E-\mu_L) - f(E-\mu_R)]\, T(E,V)dE \tag{1}$$

here, E-μ is energy w.r.t Fermi level. $f(E-\mu_L)$ & $f(E-\mu_R)$ are the Fermi-Dirac distribution of electrons at the left & right electrodes, respectively. T(E,V) is the transmission function, and the V is the bias potential. Thus, the current through the device is dependent on the transmission coefficients available within the Fermi function difference created by the applied voltages.

3. Results & Discussion

In this section, we have discussed first the geometric and electronic properties of the individual GNRs used for the channel and the electrodes, before proceeding to the device analysis.

3.1. Geometric Properties

The designed ZGNR nanoribbon and AGNR nanoribbons (N-doping, BN co-doping, N-passivation, Stone-Wales defect, and N-doping SW defect) are depicted in **Figure 2(a–g)**. The optimized C-H and C-C bond lengths of pristine GNRs are 1.10 Å and 1.42 Å, respectively. The cohesive energies (E_{Coh}) for pristine GNRs are calculated using the expression given in Equation (2) to determine the structural stability, and tabulated in **Table 1**.

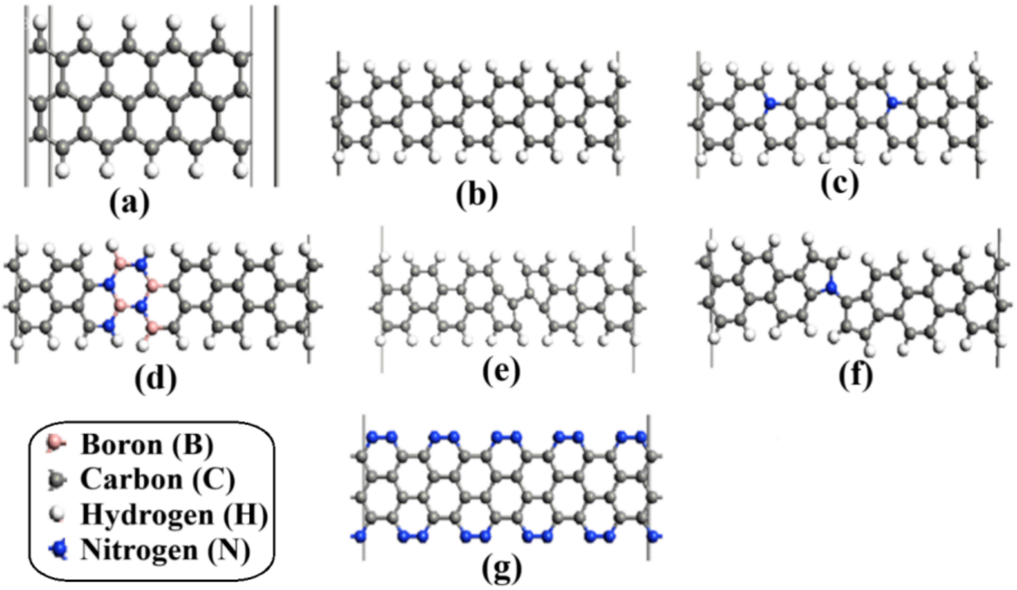

Figure 2. Optimized geometries of (**a**) Pristine ZGNR, (**b**) Pristine AGNR, (**c**) N-doped AGNR, (**d**) BN co-doped AGNR, (**e**) SW-defected AGNR, (**f**) N-Doped SW-defected AGNR, and (**g**) N-passivated AGNR. Colour Legend: Carbon (grey), Hydrogen (white), Nitrogen (blue), Boron (pink).

$$E_{Coh.} = \frac{E_{tot.} - \sum NE_x}{N} \tag{1}$$

where, $E_{tot.}$ is the total calculated energy of the nanoribbon, n_i is the number of atoms of type i, E_i is the energy of an individual isolated atom of type i, $N_{Tot.}$ is the total number of atoms in the system, i.e., $N_{Tot.} = \Sigma_i n_i E_i$ then, cohesive energies of AGNR and ZGNR are found to be −10.796 eV & −11.0458 eV, respectively, which are consistent with the literature [19]. The SW defect has been created in AGNR by rotating two carbon atoms 90 degrees to alter the electronic properties. The SW defect results in two pentagons as shown in 2(e) and 2(f). It offered a cohesive energy of −10.757 eV, indicating the retained stability of the ribbon. Similarly, the other nanoribbons N-doped AGNR, BN co-doped AGNR, N-doped SW AGNR, and N-passivated AGNR too retained their stability and offered cohesive energies of −11.584 eV, −10.666 eV, −10.749 eV, and −12.460 eV, respectively.

Table 1. Number of atoms in the channel region and the cohesive energy (E_{Coh}).

Device Channel Region	# Atoms				Total # Atoms	Cohesive Energy ($E_{Coh.}$) eV
	H	B	C	N		
AGNR	20		39		59	−10.796
N-Doped AGNR	20		37	2	59	−11.584
BN- Doped AGNR	20	4	31	4	59	−10.666
SW AGNR	20		39		59	−10.745
N-Doped SW AGNR	20		38	1	59	−10.757
N-Passivated AGNR			39	20	59	−12.460

3.2. Electronic Properties

The electronic nature of the GNRs are estimated with the help of band structure and Density of States (DOS) calculations. The band structure and DOS profiles of ZGNR are plotted in **Figure 3(a,b)**, which shows metallic nature with overlap of valence and conduction bands.

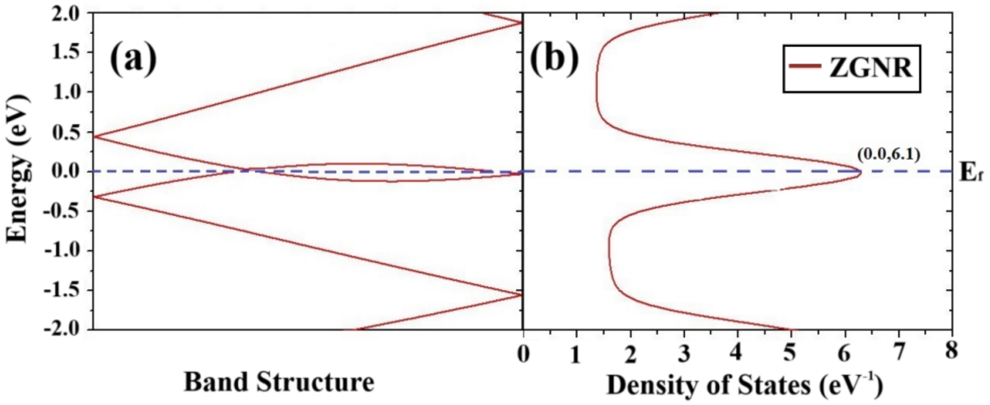

Figure 3. Band structure and Density of states (DOS) profile of Pristine ZGNR (The Fermi level is shifted to energy zero).

This electronic nature is consistent with previous findings [20,21]. Here, a DOS peak of 6.1 states/eV is observed at the Fermi level. Please note that in all the electronic structures the Fermi level is shifted to energy zero for easier discernment of the valence and conduction bands. The metallic nature of ZGNR confirms its usefulness for the present work, as it will be utilized for the source/drain electrodes of transistor. The band structure and DOS profiles of AGNR are plotted in **Figure 4(a,b)**, which shows the semiconducting nature of the nanoribbon with a band gap of 2.71 eV. The DOS peaks in the conduction band are observed to be 24.9 states/eV at 1.75 eV and 30.5 states/eV at 1.9 eV; and the same in valance band are observed to be 12.5 states/eV at −0.74 eV and 35 states/eV at −0.79 eV. This indicates the availability of large number of states at the upper edge of valence band and the lower edge of the conduction band. However, the band gap offered by the pristine AGNR is on the higher side in comparison to the conventional semiconductors used by the industry. For instance, the two mostly used semiconductors of the industry - silicon and germanium have band gaps of 1.21 eV and 0.74 eV, respectively at 0^0 K [22,23]. Thus, in order to reduce the bandgap and improve the electrical properties, a few defects and dopants are incorporated into the AGNR as discussed below.

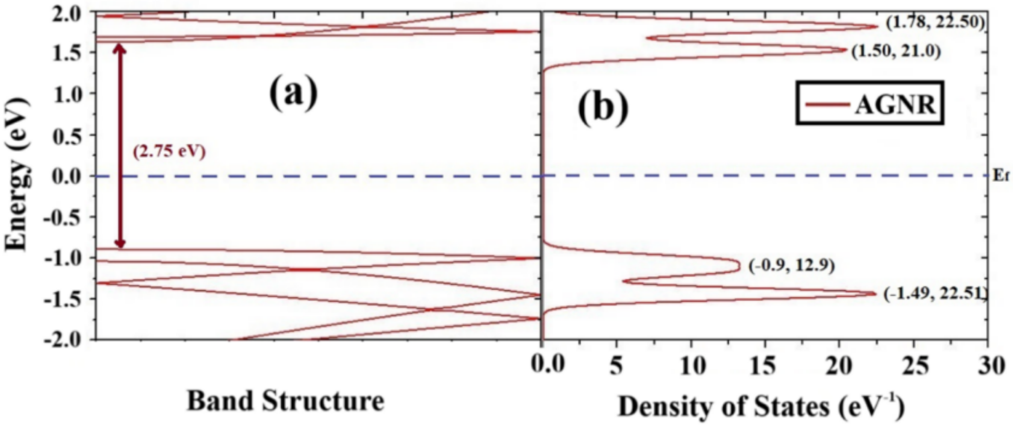

Figure 4. Band structure and DOS profile of Pristine AGNR.

The band structure and DOS profiles of N-doped AGNR are plotted in **Figure 5(a,b)**, which shows the semiconducting nature of the nanoribbon with a narrow band gap of 0.13 eV. The DOS peaks in the conduction band are observed to be 24 states/eV at 0.1 eV and 47.5 states/eV at 0.2 eV; and the same in valance band are observed to be 21.5 states/eV at −0.1 eV and 72 states/eV at −0.25 eV.

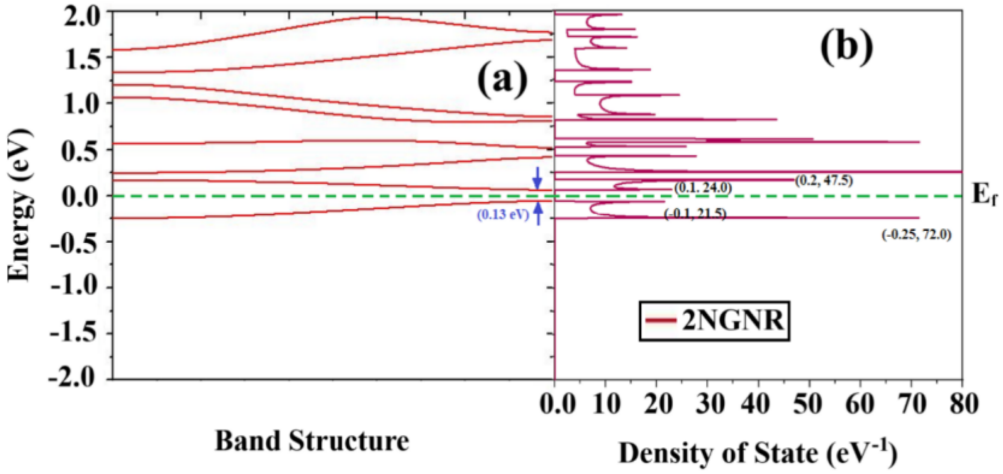

Figure 5. Band structure and DOS profile of N-doped AGNR.

This DOS profile also indicates the availability of large number of states at the upper edge of valence band and the lower edge of the conduction band. To further tune the electronic properties, we have introduced both the boron and nitrogen dopants at the same time as shown in **Figure 2(d)**. The band structure and DOS profiles of BN co-doped AGNR are plotted in **Figure 6(a,b)**, which also shows the semiconducting nature of the nanoribbon with a narrow band gap of 0.25 eV. The DOS peaks in the conduction band are observed to be 50.7 states/eV at 0.14 eV and 29.8 states/eV at 1.4 eV; and the same in valance band are observed to be 17.6 states/eV at −0.04 eV and 200 states/eV at −0.1 eV. This DOS profile also indicates the availability of large number of states at the upper edge of valence band and the lower edge of the conduction band.

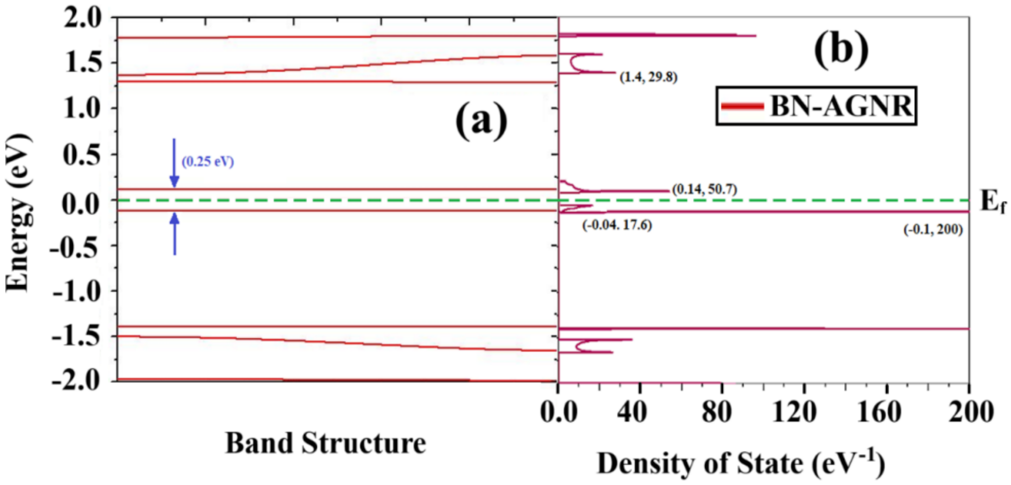

Figure 6. Band structure and DOS profile of BN co-doped AGNR.

The Stone-Wales (SW) defect is introduced into the AGNR as shown in **Figure 2(e)**. The band structure and DOS profiles of SW AGNR are plotted in **Figure 7(a,b)**, which shows the semiconducting nature of the nanoribbon with a band gap of 1.6 eV. The DOS peaks in the conduction band are observed to be 43.2 states/eV at 0.38 eV and 135.6 states/eV at 0.7 eV; and the same in valance band are observed to be 200 states/eV at −0.7 eV and 140.2 states/eV at −0.8 eV. This DOS profile also indicates the availability of large number of states at the upper edge of valence band and the lower edge of the conduction band.

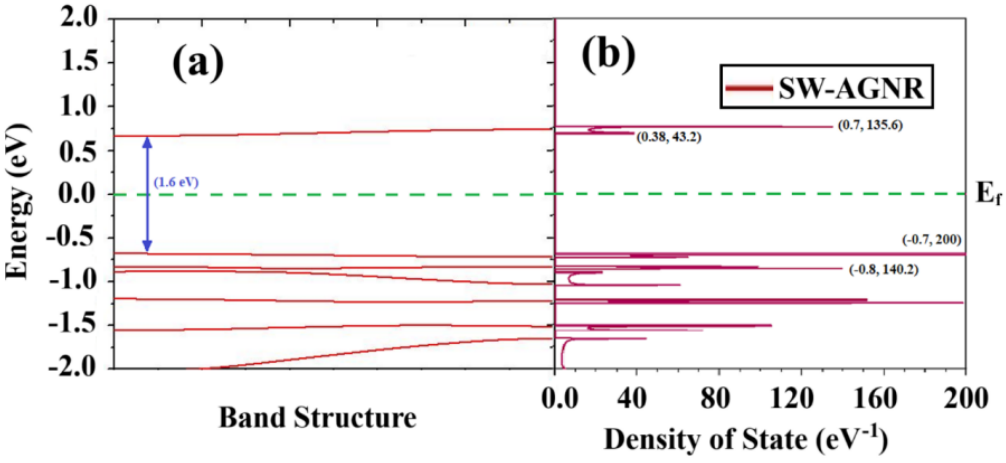

Figure 7. Band structure and DOS profile of Pristine SW AGNR.

To further tune the band gap of SW AGNR, a single nitrogen dopant has been introduced at the SW defect site as shown in **Figure 2(f)**. The band structure and DOS profiles of N-doped SW AGNR are plotted in Figure **8(a,b)**, which also shows the semiconducting nature of the nanoribbon with a good band gap of 0.58 eV. The DOS peaks in the conduction band are observed to be 290.1 states/eV at 0.1 eV and 74.8 states/eV at 1.75 eV; and the same in valance band are observed to be 312.5 states/eV at −0.6 eV and 324.4 states/eV at −1.01 eV. This DOS profile also indicates the availability of large number of states at the upper edge of valence band and the lower edge of the conduction band.

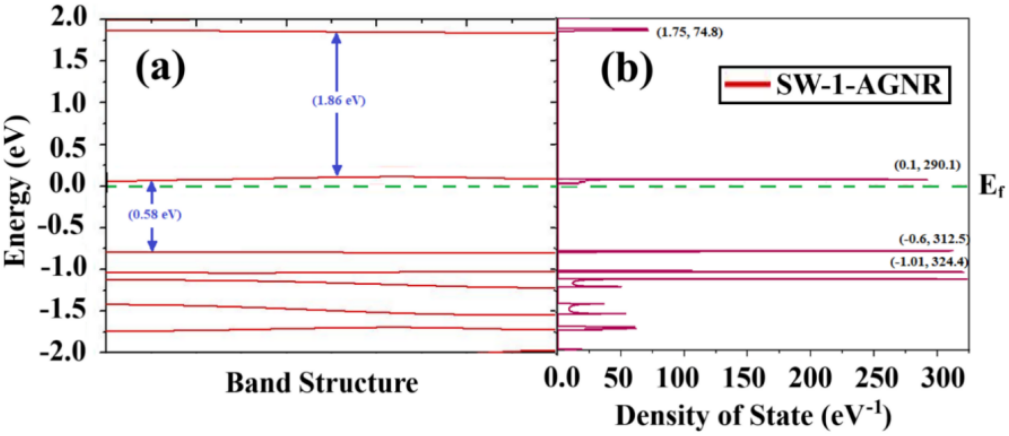

Figure 8. Band structure and DOS profile of N-doped SW AGNR.

Finally, the AGNR has been passivated with nitrogen atoms instead of hydrogen atoms. The band structure and DOS profiles of BN co-doped AGNR are plotted in **Figure 9(a,b)**, which also shows the semiconducting nature of the nanoribbon with a negligible band gap of 0.013 eV. The DOS peaks in the conduction band are observed to be 31.2 states/eV at 0.1 eV and 160 states/eV at 0.58 eV; and the same in valance band are observed to be 71 states/eV at −0.53 eV and 108.5 states/eV at −1.2 eV. This DOS profile also indicates the availability of large number of states at the upper edge of valence band and the lower edge of the conduction band. Having an idea of the electronic properties, we proceed to the device design and extraction of transport properties.

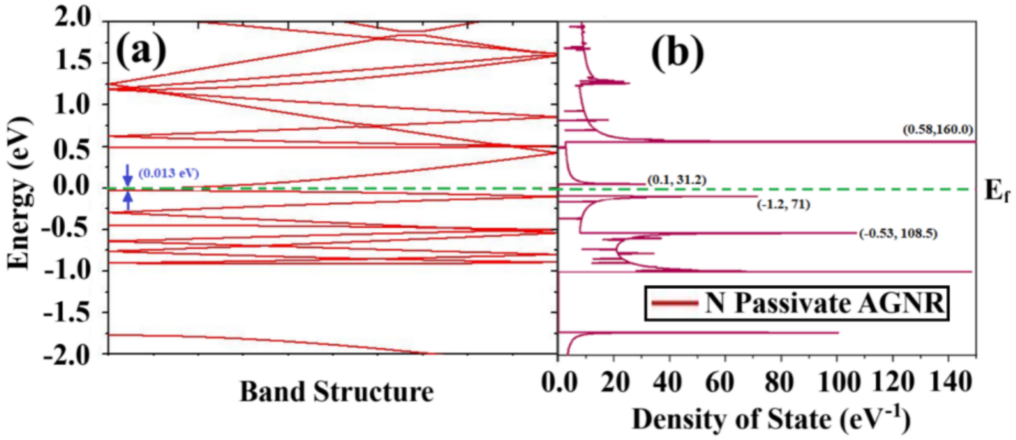

Figure 9. Band structure and DOS profile of N-Passivated AGNR.

3.3. Device and I–V Characteristics

The modelled AGNR FET with semi-infinite left/right electrode lengths of 7.358 Å and channel length of 34.454 Å is depicted in **Figure 10(a)**. The I–V characteristics of the device have been extracted from the transmission coefficients by solving the Landauer-Buttiker formula at a gate voltage of 1 V. From **Figure 10(b)**, a linear rise in the current is witnesses till V_{DS} = 0.5 V. The device also shows negative differential resistance (NDR) effect with peak voltage located at 1.6 V and valley voltage located at 2.7 V. The peak to valley current ratio is observed to be 1.33, portraying the FET as a potential candidate for the design of oscillators.

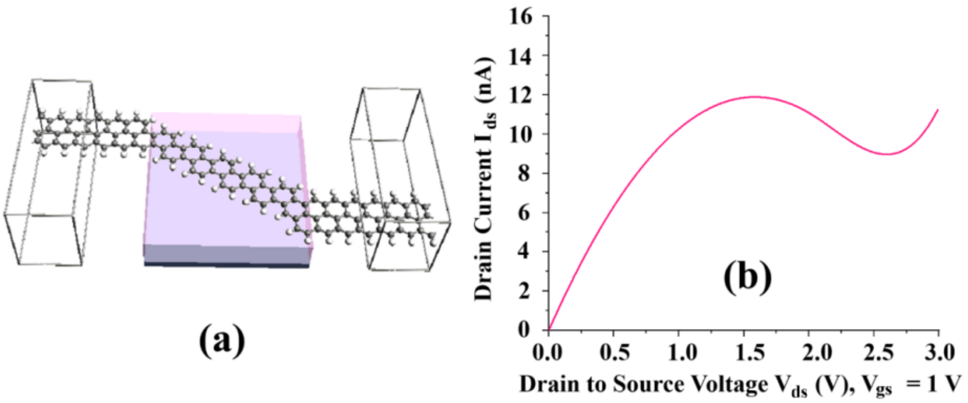

Figure 10. (**a**) FET with AGNR channel and ZGNR electrodes, (**b**) I–V curve of pristine AGNR FET.

Figure 11 presents a set of transmission spectra illustrating the Transmission Coefficient T(E) as a function of Energy (eV) under different applied bias voltages. The subfigures (a) to (d) correspond to increasing voltages: 0.5 V, 1.0 V, 1.5 V, and 2.0 V, respectively. Here, E_L and E_R indicated in the transmission spectrum represent the Fermi levels of the left and right electrodes. It is worth noting that the electrode Fermi levels shifted from energy zero by the same amount as the magnitude of applied bias voltage. The energy range between E_L and E_R is referred to as the Fermi function difference, where the presence of states is mandatory for the electron to flow left electrode to right electrode. As seen from **Figure 11**, As the bias voltage increases, the energy window expands, leading to a shift in transmission peaks and changes in the transmission spectrum structure. These modifications influence electron transport properties in the graphene nanoribbon (GNR) system, playing a crucial role in understanding quantum transport behaviour in GNR-based transistors (GNR-FETs).

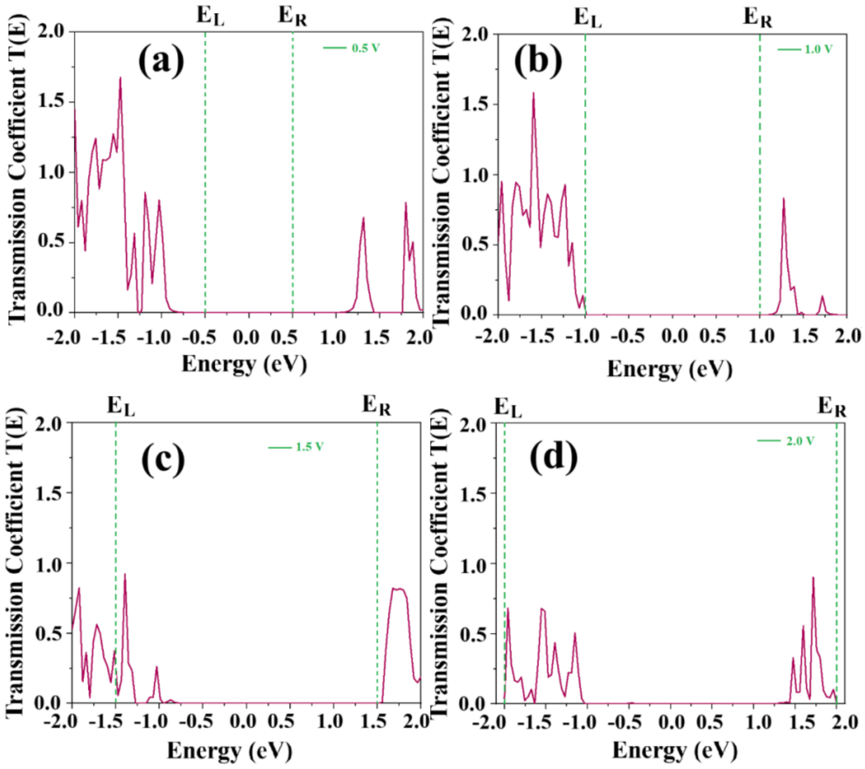

Figure 11. Transmission Spectrum of AGNR-FET (W = 4) at (**a**) 0.5 V, (**b**) 1.0 V, (**c**) 1.5 V and (**d**) 2.0 V.

Figure 12(a) compares the output I–V characteristics of the GNR FET having doped and defected AGNR channels and subfigure (b) is the zoomed view. The peak current values observed for each case is tabulated in **Table 2**. The peak drive currents offered by these channels are in the order N-passivated > N-doped SW > SW defected > N-doped > Pristine > BN co-doped. The BN co-doped AGNR FET offered the least drive current of 0.952 nA, whereas the N-passivated AGNR offered the highest drive current of 962 nA. It is worth noting that drive current offered by the N-passivated AGNR FET is about 157 times higher than the H-passivated (pristine) AGNR FET. This can be attributed to the fact that the nitrogen atoms possess lone pair of electrons in their p-orbital at the dangling bond site, while the hydrogens of pristine AGNR do not have any leftover (un-bonded) electrons. Despite it's the superior drive current, the N-passivated AGNR may not be good choice for the FET application, given its extremely low band gap of 0.013 eV. This negligible band gap can result in higher leakage currents, extremely low thermal stability, and lower peak inverse voltages. After discarding the N-passivated AGNR for FET application, the next better drive current is offered by the N-doped SW AGNR FET with a peak value of 33.21 nA. The N-doped SW AGNR offers a suitable band gap of 0.58 eV which is very close to the band gap of germanium, a commercially utilized semiconductor for FET applications. This suitable band gap of N-doped SW AGNR ensures relatively lesser leakage current, better thermal range and large peak inverse voltage. Hence, the N-doped SW AGNR may be a suitable candidate among the AGNR configurations studied in the present work for the design of next generation nanoscale FETs.

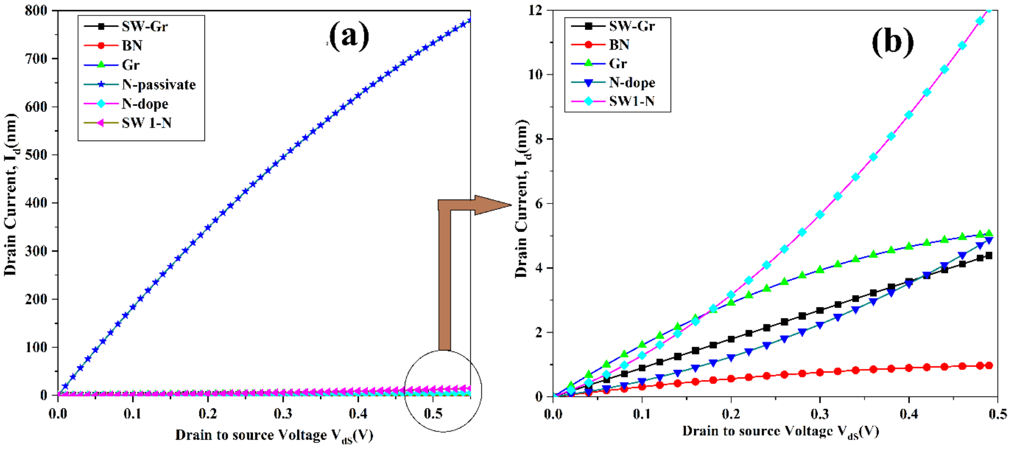

Figure 12. I–V Plot of different AGNR-FETs like BN-AGNR-FET, Pristine-AGNR-FET, N-doped AGNR-FET, N-doped SW-AGNR-FET, SW AGNR-FET and N-passivated-AGNR-FET.

Table 2. Variation in the I–V of different device's channel region.

Device's Channel Region	Drive Current $I_{d(max)}$
Pristine AGNR FET	6.1 nA
N-doped AGNR FET	12.2 nA
BN co-doped AGNR FET	0.952 nA
SW AGNR FET	16.12 nA
N-doped SW AGNR FET	33.21 nA
N-passivated AGNR FET	962 nA

4. Machine Learning Assisted Statistical Variation Analysis of N-Passivated GNR FET

Utilizing machine learning can prove invaluable in understanding the statistical variation of a novel GNR FET architecture, leading to optimized designs and improved future device performance. Recent research has explored the intriguing idea of replacing traditional numerical TCAD device simulations with a C-ANN (Conventional Artificial Neural Network) model. TCAD simulations involve complex mathematical models and algorithms to simulate semiconductor device behavior, considering various physical phenomena and process parameters [24,25]. On the other hand, neural networks possess the capacity to learn integrated patterns and relationships from data. This study aims to investigate the feasibility of replacing numerical TCAD device simulations with C-ANN, assessing whether the C-ANN model can achieve sufficient accuracy to predict device behavior without relying on TCAD simulations by doing so, this approach may offer a faster and more efficient means of evaluating device characteristics and aiding in the design optimization process.

This study explores the potential of replacing numerical TCAD device simulations with a C-ANN model to predict device behavior accurately. To achieve this, simulated data from TCAD was used to train the C-ANN. The dataset consisted of 3,000 samples of I_{ON} values from best result (N-Passivated GNR FET) devices, with 70% of the data utilized for training the neural networks, 15% for testing, and another 15% for validation. The performance of the ML-assisted analysis was assessed using the remaining 15% data as a validation set. The C-ANN architecture employed in this work is a fully connected neural network with 5 inputs, 3 hidden layers, and 3 outputs, as depicted in **Figure 13.** Leaky ReLU was chosen as the activation function for the hidden layers, and stochastic gradient descent (SGD) was used as the optimizer to minimize the objective function. Notably, the conventional-ANN needed to be trained from an initialized state, involving setting appropriate weights and biases to optimize its performance. The ML-assisted modeling framework leverages deep learning techniques to enhance the accuracy and efficiency of the predictions, and a batch size of 42 was utilized for the input data during training [26].

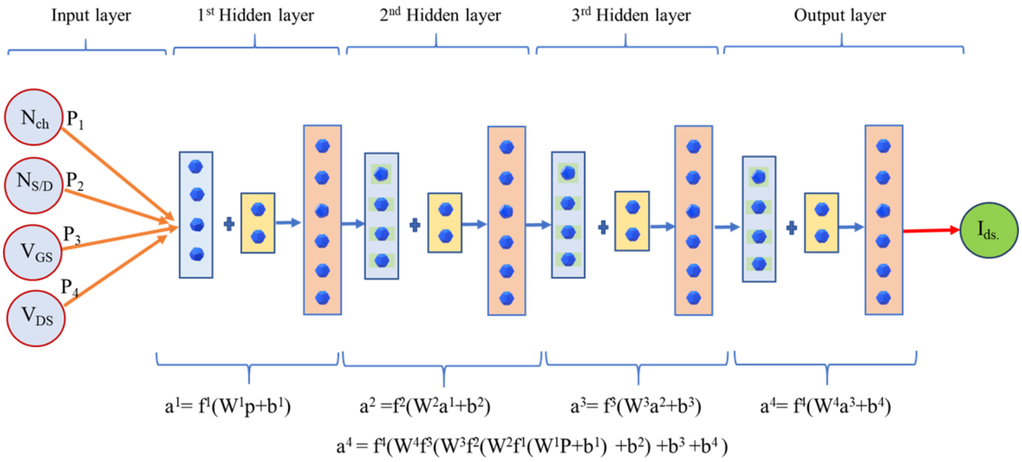

Figure 13. Fully Connected CANN structure used for ML-based prediction.

Mean Square Error (MSE) serves as a widely-used loss function to assess the regression model's performance, including Conventional Artificial Neural Networks (C-ANNs). In this study, MSE is employed as the primary metric to evaluate the accuracy of the trained C-ANN. The MSE values for N passivate GNR FET has been consistently reduced during training, eventually reaching a stable state. **Figure 14.** illustrates the MSE trends, where the blue line represents training values, the green line denotes data validation, the red line corresponds to test values, and the dotted line indicates the best MSE value 0.036347 has been achieved. Smaller MSE values indicate improved performance of the C-ANN, as they signify a smaller average difference between the predicted and actual values. Furthermore, **Figure 15.** displays a graphical representation of the dataset's distribution of errors or residuals specifically, it shows the comparison between the predicted I_{ds} values from the C-ANN and the true values of Ids obtained from the numerical device simulation. This visualization provides insights into the model's accuracy in predicting device behavior and helps validate the effectiveness of the ML-assisted analysis [26]. In general, when the predicted value of I_{ds} perfectly matches the true value of I_{ds}, each grey dot should lie exactly on top of the red and blue lines. In this proposed work, the predicted values are very close to the true values, which is indicated by the correlation coefficient (R) values. The R is a commonly used metric for training, validation, testing, and evaluating neural networks. The obtained values of correlation coefficient (R) for the proposed work (Training = 0.93417, Test = 0.97823, Validation = 0.98047, All = 0.94687) reflect a strong correlation and indicate the effectiveness of the C-ANN model in accurately approximating device behavior [27–34].

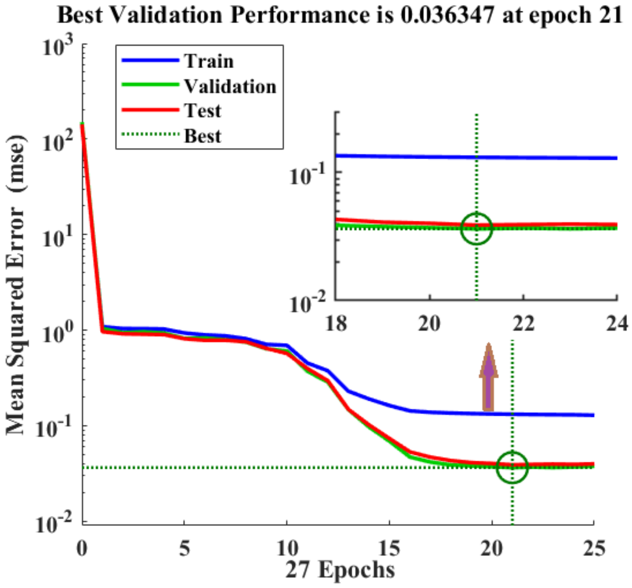

Figure 14. Mean square error values for proposed methodology.

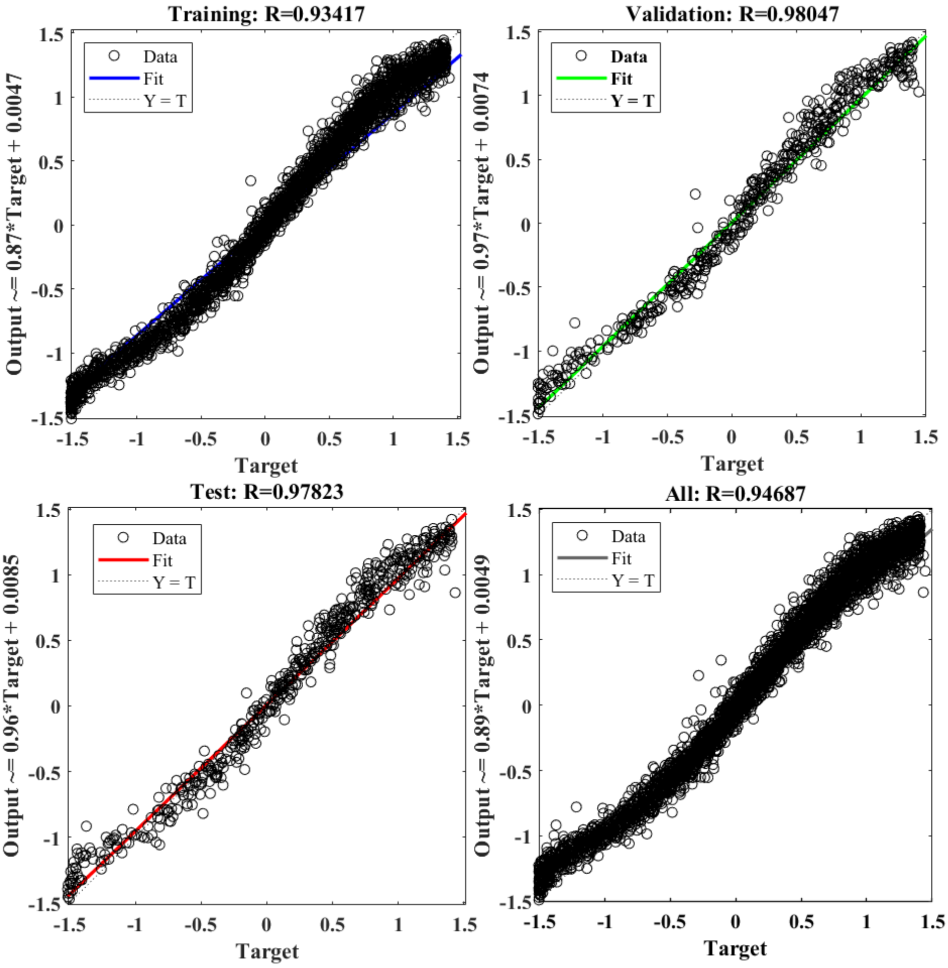

Figure 15. True values vs predicted values for the Ids of proposed device with the help of C-ANN of N-Passivate GNR FET.

In the context of C-ANNs, the distribution of errors can offer valuable insights into the network's performance and the dataset's characteristics. **Figure 16** presents a bar graph illustrating the errors between the predicted and true values of I_{ds} for the tested dataset. The shape of the error histogram curve closely follows a Gaussian distribution, indicating the successful training of the C-ANN with the dataset. The Gaussian-like distribution signifies that the C-ANN has learned to capture the underlying patterns and relationships in the data, leading to accurate predictions. This observation further validates the effectiveness of the ML-assisted approach in approximating device behavior and reinforces the suitability of using the C-ANN as a viable alternative to numerical TCAD device simulations.

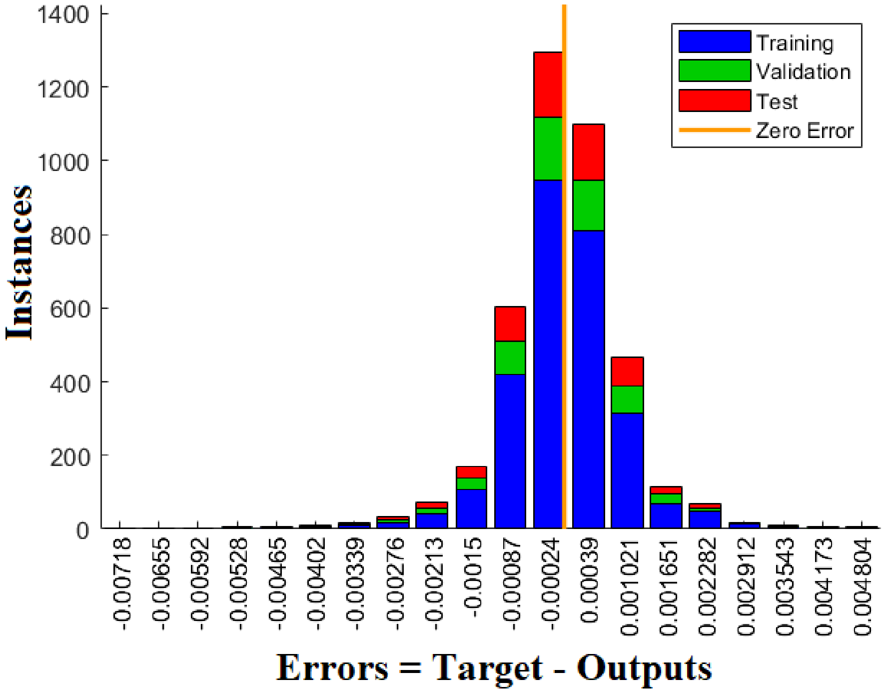

Figure 16. Error Histogram for the proposed C-ANN of N-Passivate GNR FET.

5. Conclusions

This work summaries a unique GNR FET utilizing Zigzag GNRs (ZGNRs) as electrodes and Armchair GNRs (AGNRs) as the channel, analyzed using Extended-Hückel formalism and Landauer-Buttiker transport theory. Electronic structure investigations reveal a pristine AGNR band gap of 2.71 eV, which is tunable between 0.013 eV and 1.6 eV through doping and defect engineering. Transport analysis highlights an N-passivated AGNR FET with a drive current 157× higher than pristine AGNR FET, though its negligible band gap risks high leakage current. In contrast, the N-doped Stone-Wales (SW) AGNR FET achieves an optimal 33.21 nA drive current with a 0.58 eV band gap, ensuring lower leakage, better thermal range, and higher peak inverse voltage, making it a strong candidate for next-generation GNR-based nano-transistors. To accelerate device analysis, a Machine Learning (ML)-assisted approach using a Conventional Artificial Neural Network (C-ANN) is introduced, drastically reducing computational time. By considering only 20 drain voltage variations, C-ANN simulates the Id–Vg curve in just 150–170 seconds, compared to the 60–64 days required by the COGENDA TCAD simulator for 4,000 samples. This first-ever ML application in Low Power GNR-FETs highlights the efficiency and reliability of C-ANN, revolutionizing nano-device simulations with fast, accurate predictions.

Author Contributions

Conceptualization, A.P.; Writing original draft, A.P.; Methodology, A.P.; Data curation. A.P.; review & editing, S.S.; formal analysis. S.S.; Supervision, R.K.; review & editing, S.Y.; formal analysis, S.Y. All authors have read and agreed to the published version of the manuscript.

Funding

This work does not receive any type of funding.

Institutional Review Board Statement

Not applicable.

Informed Consent Statement

Not applicable.

Data Availability Statement

Data will be made available on request.

Acknowledgments

The authors are grateful to the Microelectronics Research Laboratory, Department of Electronics and Communication Engineering, Maulana Azad National Institute of Technology, Bhopal (462003), Madhya Pradesh India, for supporting the work.

Conflicts of Interest

We declare that we do not have any commercial or associative interest that represents a conflict of interest in connection with the work submitted.

References

1. Granzner, R.; Schwierz, F.; Polyakov, V.M. An analytical model for the threshold voltage shift caused by two-dimensional quantum confinement in undoped multiple-gate MOSFETs. *IEEE Trans. Electron Devices* **2007**, *54*, 2562–2565.
2. Guo, J. Modeling of graphene nanoribbon devices. *Nanoscale* **2012**, *4*, 5538–5548.
3. Llinas, J.P.; Fairbrother, A.; Barin, G.B.; et al. Short-channel field-effect transistors with 9-atom and 13-atom wide graphene nanoribbons. *Nat. Commun.* **2017**, *8*, 1–6.
4. Singh, A.P.; Shankar, P.N.; Baghel, R.; et al. A Review on Graphene Transistors. In Proceedings of 2023 IEEE International Students' Conference on Electrical, Electronics and Computer Science (SCEECS), Bhopal, India, 18–19 February 2023.
5. Son, J.G.; Son, M.; Moon, K.-J.; et al. Sub-10 nm Graphene Nanoribbon Array Field-Effect Transistors Fabricated by Block Copolymer Lithography. *Adv. Mater.* **2013**, *25*, 4723–4728.
6. Sun, D.-M.; Liu, C.; Ren, W.-C.; et al. A review of carbon nanotube-and graphene-based flexible thin-film transistors. *Small* **2013**, *9*, 1188–1205.
7. Ren, H.; Li, Q.X.; Su, H.B.; et al. Edge effects on the electronic structures of chemically modified armchair graphene nanoribbons. Available online: https://arxiv.org/abs/0711.1700 (accessed on 10 May 2007).
8. Nguyen, G.D.; Toma, F.M.; Cao, T.; et al. Bottom-up synthesis of N = 13 sulfur-doped graphene nanoribbons. *J. Phys. Chem. C* **2016**, *120*, 2684–2687.
9. Carbonell-Sanroma, E.; Garcia-Lekue, A.; Corso, M.; et al. Electronic properties of substitutionally boron-doped graphene nanoribbons on a Au (111) surface. *J. Phys. Chem. C* **2018**, *122*, 16092–16099.
10. Houtsma, R.S.K.; de la Rie, J.; Stöhr, M. Atomically precise graphene nanoribbons: interplay of structural and electronic properties. *Chem. Soc. Rev.* **2021**, *50*, 6541–6568.
11. Ruffieux, P.; Wang, S.Y.; Yang, B.; et al. On-surface synthesis of graphene nanoribbons with zigzag edge topology. *Nature* **2016**, *531*, 489–492.
12. Rui, C.K.; Shao, C.; Liu, J.X.; et al. Transport properties of B/P doped graphene nanoribbon field-effect transistor. *Mater. Sci. Semicond. Process.* **2021**, *130*, 105826.
13. Lin, M.-W.; Ling, C.; Zhang, Y.Y.; et al. Room-temperature high on/off ratio in suspended graphene nanoribbon field-effect transistors. *Nanotechnol.* **2011**, *22*, 265201.

14. Hur, J.-H.; Kim, D.-K. Theoretical investigation of performance of armchair graphene nanoribbon field effect transistors. *Nanotechnol.* **2018**, *29*, 185202.
15. Woo, S.; Jeon, J.; Kim, S. Prediction of Device Characteristics of Feedback Field-Effect Transistors Using TCAD-Augmented Machine Learning. *Micromachines* **2023**, *14*, 504.
16. Ghoshhajra, R.; Biswas, K.; Sarkar, A. A review on machine learning approaches for predicting the effect of device parameters on performance of nanoscale MOSFETs. In Proceedings of 2021 Devices for Integrated Circuit (DevIC), Kalyani, India, 19–20 May 2021.
17. Liu, D.C.; Nocedal, J. On the limited memory BFGS method for large scale optimization. *Math. Prog.* **1989**, *45*, 503–528.
18. Datta, S. Exclusion principle and the Landauer-Büttiker formalism. *Phys. Rev. B* **1992**, *45*, 1347.
19. Zhang, W.; Ragab, T.; Zhang, J.; et al. Impact of Electrostatic Doping Level on the Dissipative Transport in Graphene Nanoribbons Tunnel Field-Effect Transistors. *Carbon* **2019**, *153*, 120–126.
20. Singh, S.; Kaur, I. Bandgap engineering in armchair graphene nanoribbon of zigzag-armchair-zigzag based Nano-FET: A DFT investigation. *Phys. E: Low-dimensional Syst. Nanostruct.* **2020**, *118*, 113960.
21. Wu, Y.; Lin, Y.M.; Bol, A.A.; et al. High-frequency, scaled graphene transistors on diamond-like carbon. *Nature* **2011**, *472*, 74–78.
22. Kim, T.-Y.; Park, N.-M.; Kim, K.-H.; et al. Quantum confinement effect of silicon nanocrystals in situ grown in silicon nitride films. *Appl. Phys. Lett.* **2004**, *85*, 5355–5357.
23. Varshni, Y.P. Temperature dependence of the energy gap in semiconductors. *Phys.* **1967**, *34*, 1495154.
24. Singh, A.P.; Baghel, R.K.; Tirkey, S. Ferroelectric Based Low Power MOSFET for DC/RF Applications: Machine Learning Assisted Statistical Variation Analysis. *ECS J. Solid State Sci. Technol.* **2024**, *13*, 043011.
25. Choe, G.; Ravindran, P.V.; Hur, J.; et al. Machine learning-assisted statistical variation analysis of ferroelectric transistor: From experimental metrology to adaptive modeling. *IEEE Trans. Electron Devices* **2023**, *70*, 2015–2020.
26. Singh, A.P.; Chauhan, V.; Baghel, R.K.; et al. Enhancing VLSI Design Efficiency With ML-Based C-ANN: Performance Optimization of Gate-Stacked Ferroelectric FE-MOSFETs for High-Speed and RF Applications. *Int. J. Numer. Model.* **2025**, *38*, e70064.
27. Singh, A.P.; Baghel, R.K.; Tirkey, S. Integration of Machine Learning with Statistical Variation Analysis for Ferroelectric Transistor (FE-MOSFETs). *Mater. Open* **2024**, *2*, 2440001.
28. Yadav, S.; Shukla, A.K.; Nehete, H.; et al. Variation analysis of spintronic device using machine learning algorithm. In Proceedings of Spintronics XVI, San Diego, CA, USA, 2023; pp 20–24.
29. Yadav, S.; SanthiBhushan, B.; Srivastava, A. Carbon & boron substituted-Dibenzo [1,4] azaborinine as a quantum dot-based organic molecular single-electron device for high switching speed applications. *Mater. Today Proc.* **2022**, *48*, 666–671.
30. Katta, S.S.; Yadav, S.; Singh, A.P.; et al. Investigation of pristine and B/N/Pt/Au/Pd doped single-walled carbon nanotube as phosgene gas sensor: A first-principles analysis. *Appl. Surf. Sci.* **2022**, *588*, 152989.
31. Yadav, S.; Singh, M.; Chaudhary, T.; et al. GaAs Nanowire Field Effect Transistor. In *Integrated Devices for Artificial Intelligence and VLSI*; Raj, B., Tripathi, S.L., Chaudhary, T., et al., Eds.; Wiley: Oxford, UK, 2024; Volume 4, pp. 75–99.
32. Maurya, A.; Yadav, S.; Kishor, K.; et al. 2D-Transitional Metal Dichalcogenide Materials for Bio-sensors Application: A DFT-based approach. In Proceedings of 2024 28th International Symposium on VLSI Design and Test (VDAT), Vellore, India, 1–3 September 2024.
33. Yadav, S.; Kaushik, B.K.; Giri, A. Energy-Efficient Hybrid STT-MTJ/CMOS Circuit for Machine Learning-Assisted Neuromorphic Computing Applications. *IEEE Can. J. Electr. Comput. Eng.* **2025**, *48*, 184–191.
34. Yadav, S.; Giri, N.; Maurya, A.; et al. Machine learning and explainable-AI based prediction of gate-all-around ferroelectric-FET: how ML models influence XAI. *Phys. Scr.* **2025**, *100*, 056006.